

Advancing Galaxy Analysis: AI-Powered Detection and Segmentation of Edge-On Galaxies

Ž. Chrobáková,¹* V. Krešňáková,² R. Nagy³ J. Gazdová² and P. Butka²

¹Mullard Space Science Laboratory, University College London, Holmbury St Mary, Dorking, Surrey RH5 6NT, UK

²Department of Cybernetics and Artificial Intelligence, Faculty of Electrical Engineering and Informatics, Technical University of Kosice, 042 00 Košice, Slovakia

³Faculty of Mathematics, Physics, and Informatics, Comenius University, Mlynská dolina, 842 48 Bratislava, Slovakia

Accepted XXX. Received YYY; in original form ZZZ

ABSTRACT

Edge-on galaxies have many important applications in galactic astrophysics, but they can be difficult to identify in vast amounts of astronomical data. To facilitate the search for them, we have developed a deep learning algorithm designed to identify and extract edge-on galaxies from astronomical images. We utilised a sample of edge-on spiral galaxies from the Galaxy Zoo database, retrieving the corresponding images from the Sloan Digital Sky Survey (SDSS). Our dataset comprises approximately 16,000 galaxies, which we used to train the YOLOv5 algorithm for detection purposes. To isolate galaxies from their backgrounds, we trained the SCSS-Net neural network to generate segmentation masks. As a result, our algorithm detected 8,000 edge-on galaxies, for which we compiled a catalogue including their parameters obtained from the SDSS database. We describe the basic properties of our sample, finding that most galaxies have redshifts $0.02 < z < 0.10$, have low values of b/a and are mostly red, which is expected from edge-on galaxies and is consistent with our training sample, as well as other literature. The cutouts of the detected galaxies can be used for future studies and the algorithm can be applied to data from future surveys as well.

Key words: galaxies: disc – galaxies: general – galaxies: fundamental parameters

1 INTRODUCTION

Edge-on galaxies are of great interest due to their unique orientation that enables us to study various phenomena. They come in many types and shapes, ranging from from bulge-dominated early-type galaxies to poorly understood bulgeless galaxies (Kautsch et al. 2006). Their structure is usually studied by decomposition into parts (e.g., Kormendy & Bruzual 1978; Burstein 1979; Hamabe et al. 1979; Tikhonov & Galazutdinova 2005; Comerón et al. 2011; Salo et al. 2015), but they are also ideal for probing vertical and radial galactic structure (e.g., van der Kruit & Searle 1981; Barteldrees & Dettmar 1994; de Grijs & van der Kruit 1996; Seth et al. 2005; Bizyaev et al. 2014), measuring the rotation curve (e.g., Makarov et al. 1999; Vergani et al. 2003; Kregel & van der Kruit 2004; O’Brien et al. 2023) or investigating stellar haloes (e.g., Zibetti & Ferguson 2004; Mouhcine et al. 2007; Mosenkov et al. 2020; Gilhuly et al. 2022). Edge-on galaxies are also suitable for observing peculiar features, such as galactic warps (e.g., Sancisi 1976; Reshetnikov & Combes 1998; Zee et al. 2022), disc truncation (e.g., Pohlen et al. 2000, 2002; van der Kruit 2007; Martínez-Lombilla et al. 2019), galactic fountains (Bregman 1980; Bregman & Houck 1997; Fraternali et al. 2005; Hodges-Kluck & Bregman 2012) or extraplanar gas (Pildis et al. 1994; Lee & Irwin 1997; Levy et al. 2019; Reach et al. 2020) and extraplanar dust (e.g., Howk & Savage 1997, 1999; Shinn 2018; Mosenkov et al. 2022) among others.

With the increasing volume of data from various surveys, machine learning (ML) is becoming a necessity in galaxy analysis. There are

many examples of using machine and deep learning for classifying galaxies based on their morphology (e.g., Storrie-Lombardi et al. 1992; Banerji et al. 2010; Dieleman et al. 2015; González et al. 2018; Barchi et al. 2020; Gharat & Dandawate 2022, just to name a few), or from spectra, which enables the detection of active galactic nuclei (AGNs), star-forming or other galaxies (e.g., Shi et al. 2015; Zhang et al. 2019; Peruzzi et al. 2021; Wu et al. 2024). In the galactic context, ML can also be used to estimate redshift (e.g., Collister & Lahav 2004; Bonnett 2015; D’Isanto & Polsterer 2018; Lin et al. 2022), identify galaxy-scale gravitational lensing (e.g., Cheng et al. 2020; Rezaei et al. 2022; Wilde et al. 2022; Andika et al. 2023), classify galaxy mergers (e.g., Pearson et al. 2019; Ferreira et al. 2020; Chang et al. 2022; Omori et al. 2023), estimate various galaxy parameters (e.g., Bonjean et al. 2019; Surana et al. 2020; Liew-Cain et al. 2021; Davidzon et al. 2022; Ghosh et al. 2022; Chu et al. 2024; La Torre et al. 2024), extract features (e.g., Abraham et al. 2018; Ghosh et al. 2020; Tarsitano et al. 2022; ?) and for other applications.

The application of ML algorithms specifically for detecting edge-on galaxies has just recently started to get explored. Savchenko et al. (2024) trained an artificial neural network (ANN) on edge-on galaxies extracted from the catalogue of genuine edge-on disc galaxies (EGIS, Bizyaev et al. 2014). Then they applied the algorithm on the data from the Panoramic Survey Telescope and Rapid Response System (Pan-STARRS, Kaiser et al. 2010), where they detected $\sim 10^5$ galaxies with a detection rate of about 97%. Makarov et al. (2022) analysed the properties of this sample, finding that red sequence galaxies are thicker than the galaxies of the blue cloud and edge-on galaxies are systematically redder than the general population of

* E-mail: z.chrobakova@ucl.ac.uk

galaxies seen at arbitrary angles. [Usachev et al. \(2024\)](#) applied this ANN algorithm on images from the Hubble Space Telescope COSMOS field ([Scoville et al. 2007](#)), where they detected 950 edge-on galaxies. They studied their scale-lengths and scale-heights, finding that their evolution is luminosity-dependent.

In this work, we develop a deep learning algorithm which combines detection of edge-on, spiral galaxies followed by cutting them off (using segmentation) from the image automatically, so they are prepared for any further scientific analysis. This paper is structured as follows. In Section 2, we describe the selection of images, which were used for the algorithm training. In Section 3, we explain the algorithm and its performance in detail. In Section 4 we present our detected sample and its basic properties. In Section 5 we summarise our findings.

2 DATA SELECTION

We are interested in detecting edge-on, spiral galaxies. Galaxies that are not completely edge-on, but are highly inclined are also appropriate, but for simplicity we will refer to our whole sample as edge-on. We selected our original sample from the Galaxy Zoo project ([Lintott et al. 2008](#)) and we downloaded the primary Galaxy Zoo 2 sample ([Willett et al. 2013](#)), which contains classifications of the 243,500 galaxies in the main sample with spectroscopic redshifts. From this sample, following the criteria of [Zee et al. \(2022\)](#), we selected those galaxies, that at least one half of the volunteers voted to be edge-on and at least 80% of the volunteers voted to be spiral galaxies. Then we retrieved the fits of these selected galaxies from the The Sloan Digital Sky Survey (SDSS) Data release 7 ([Abazajian et al. 2009, DR7](#)) Legacy Survey, which is the final data release of the SDSS Legacy Survey. We used all available fits files of all selected galaxies in all filters, so for most galaxies, we have several images. Those are treated as separate objects by the ML algorithm.

Once the images were selected (15,500 fits files), they were uploaded to the Zooniverse¹ platform, which became an important component of our data annotation process. The choice of Zooniverse was because of its proven track record in facilitating effective crowd-sourced scientific research, offering tools that simplify the complex tasks of data annotation for non-experts. This platform provided an intuitive interface for volunteers to interact with the data directly, ensuring that the annotations were accurate and verifiable. Volunteers were first presented with a brief tutorial explaining the characteristics of edge-on spiral galaxies and how to identify them. This tutorial included examples of images they would encounter and step-by-step instructions on how to mark the galaxies using the tools provided by the platform. The data collected through this method were then compiled and prepared for the next stages of our research, focusing on developing a machine learning algorithm to automate the detection of spiral galaxies. In the end, we have 16,701 galaxies in 9,023 fits files. An example of an annotated image is shown in Fig. 1.

3 ALGORITHM

Our algorithm for deep learning based extraction of edge-on galaxies, followed by acquisition of scientific data about detected objects, consists of three separated steps as part of main processing pipeline:

¹ <https://www.zooniverse.org/>

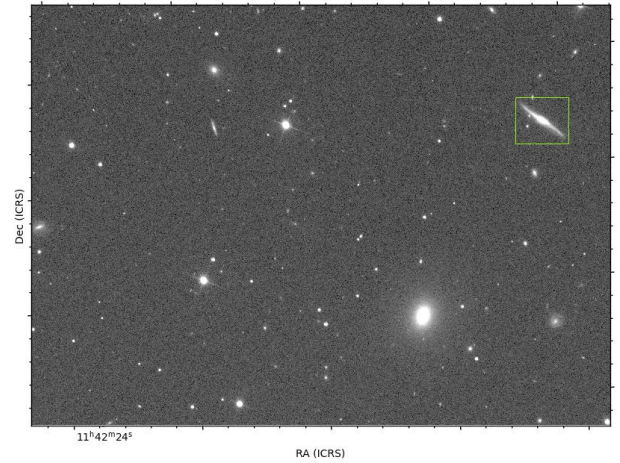


Figure 1. An example of an edge-on spiral galaxy annotated with a green bounding box by a volunteer.

- (i) **Detection** - in this step we acquire detection boxes of edge-on galaxies based on the results from YOLOv5 detection model, trained on selected data from SDSS survey.
- (ii) **Segmentation** - extraction of cutouts of detected galaxies using retrained U-Net-based architecture.
- (iii) **Data Extraction** - in this step, segmented masks are used to extract data from fits only for segmented edge-on galaxy, as well as cross-match detected galaxy with SDSS or other catalogues to extract selected parameters.

We provide more details on all three steps in next subsections.

3.1 YOLOv5 Training and Evaluation

In our study, we utilised a dataset consisting of 9,023 annotated images featuring galaxies. We divided this dataset into three subsets: training (70%), validation (15%), and testing (15%). The training set, comprising 6,314 images, was used to train the YOLOv5 model ([Jocher et al. 2020](#)). The validation set, with 1,354 images, helped evaluate the learning progress of the model. The testing set, which includes 1,353 images, was used for the final model evaluation. It is important to note that if a galaxy appears in different filters, all versions of that galaxy are included in the same subset. This ensures that the same galaxy does not appear in multiple subsets. From a machine learning perspective, the different filters can be considered as data augmentations, which are very beneficial; however, this condition must be met to maintain the integrity of the data distribution.

To prepare the data for YOLOv5, we focused on three key columns: metadata, subject_data, and annotations, extracting essential annotation information. A Python script generated the necessary text files for YOLOv5, containing labels and normalised coordinates x and y , where the centre of the coordinate system $x, y = (0, 0)$ is in the upper left corner of the image. The coordinates were normalised using the following formulas:

$$\text{norm_x} = \frac{x + \frac{\text{width}}{2}}{\text{picture_width}} \quad (1)$$

$$\text{norm_y} = \frac{y + \frac{\text{height}}{2}}{\text{picture_height}} \quad (2)$$

Table 1. Table with metrics calculated by YOLOv5 on testing dataset. One image may contain more than 1 instance of edge-on galaxy. Precision and Recall are calculated according to TP, FP and FN values (see Table 2).

Images	Instances	Precision	Recall
1353	1892	0.80	0.94

Each text file corresponds to an image, with multiple galaxy annotations recorded on separate lines within the same file if present.

The YOLOv5 detection model follows a structured architecture comprising three main parts: Backbone, Neck, and Head. The Backbone part (CSPDarkNet) extracts important features from images. The Neck part refines these features, often utilising Feature Pyramid Networks (FPN) to enhance spatial and semantic information. The Head part processes these outputs to produce bounding box predictions (detection boxes) and object classes. This architecture ensures efficient and accurate real-time object detection, often used in practice for image processing, making YOLOv5 a robust choice for our galaxy detection step (Jocher et al. 2020; Redmon et al. 2016; Vijayakumar & Vairavasundaram 2024).

We used several key metrics to evaluate the performance of our YOLOv5 model:

- **Confusion Matrix:** In general, it is a table or set of numbers which presents the performance of the prediction models by providing number of cases considered as True Positive (TP), False Positive (FP), False Negative (FN) and True Negative (TN) predictions. Due to the nature of detection tasks, where TNs represent the background without the expected detection and are thus not relevant, only the first three metrics are applicable and of interest, where:

- TP is number of cases when object (edge-on galaxy in our case) was annotated for detection and was also correctly detected by the model,
- FP is number of cases when object was not annotated, but was detected by the model,
- FN is number of cases when object was annotated, but model did not detect it.

- **Precision:** The ratio of correctly predicted positive observations (TP) to the total predicted positives (TP and FP), calculated as:

$$\text{Precision} = \frac{\text{TP}}{\text{TP} + \text{FP}} \quad (3)$$

- **Recall:** The ratio of correctly predicted positive observations (TP) to all observations in the actual class (TP + FN), calculated as:

$$\text{Recall} = \frac{\text{TP}}{\text{TP} + \text{FN}} \quad (4)$$

Precision and Recall, based on the confusion matrix elements, are metrics which provide comprehensive evaluation of the performance of the model in detecting edge-on galaxies.

For the detection task, we used a manually annotated set of images from SDSS. The annotation was performed by the students using the Zooniverse platform. The results of the performance of the YOLOv5 model on the test set are summarised in Table 1. The table shows the number of images and its instances of edge-on galaxies, along with the key metrics: Precision and Recall. These results indicate that the model performs well in detecting edge-on galaxies, with a balanced trade-off between precision and recall.

To provide a comprehensive understanding of the performance of the YOLOv5 model, we also provide particular detection cases, where we can see the sources of errors more precisely. Table 2

Table 2. Summary of TPs, FPs, and FNs identified by the YOLOv5 detection model.

Detection case	Count
True Positives (TP)	1783
False Positives (FP)	442
False Negatives (FN)	113

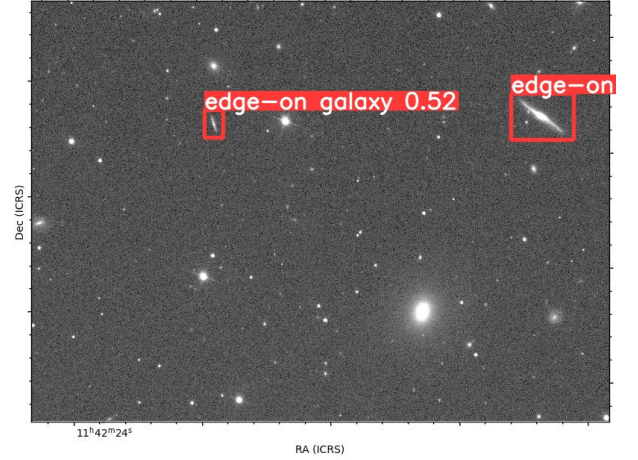


Figure 2. The same image as Fig. 1, but showing the galaxies detected by the YOLOv5 detection model. There is one extra galaxy identified, compared to the annotation.

summarises the counts of TP, FP, and FN, which are essential for estimating the detection capabilities of the model.

Due to manual annotations by students, there is some inevitable annotation bias, e.g., not every time students annotated all instances or sometimes a wrong object was annotated. One of the advantages of deep learning techniques is their ability to overcome annotation bias issues and provide correct predictions even for cases with annotation mistakes. This is possible if annotations are generally correct for most cases and the architecture is able to learn a good generalised prediction function. Hence, the real efficiency of algorithm is even better and might be additionally estimated by the analysis of wrong cases.

According to our knowledge from the Galaxy Zoo project, there should be at least one edge-on galaxy in the image, but that does not rule out the possibility of detecting other galaxies. Initially, our annotators only flagged galaxies that they were confident of, but our algorithm successfully detected several others. This is illustrated in Fig. 2, where we present an example image that initially had one galaxy annotation from Zooniverse (see Fig. 1). After applying our YOLOv5 model, an additional galaxy was detected. This demonstrates the capability of the model to identify galaxies that may have been missed in the initial annotations due to manual annotation bias.

To verify these findings, we manually examined detections labeled as FP and FN. Figures 3 and 4 show cases of FPs and FNs, providing visual context for these detections.

Through visual inspection, we found that a number of misclassifications are due to inaccuracies in the annotation. In more detail, at least $\sim 20\%$ of the FP cases are considered edge-on galaxies, which were not annotated by mistake, and therefore these cases might be relocated from FP to TP after such analysis. For another $\sim 20\%$ of galaxies we were not able to decide, based on visual inspection, what their inclination is, but some of them might be edge-on as well. Hence, we can estimate that Precision is probably at least $\sim 85\%$

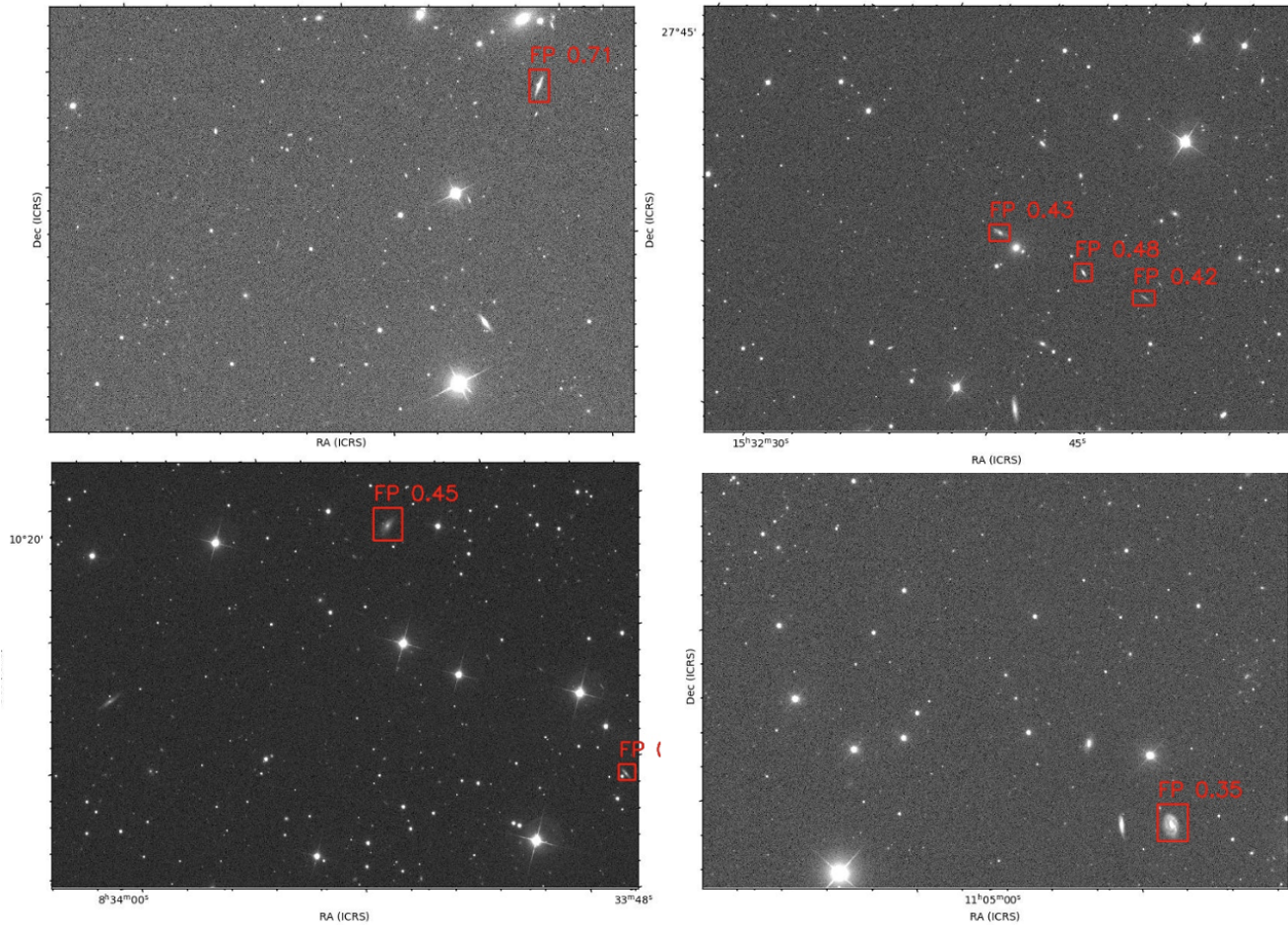


Figure 3. Examples of False Positives Detected by YOLOv5. We can see that the model’s ability to identify galaxies that were often missed in the initial annotations and these objects might be considered as True Positives instead of False Positives.

in comparison to $\sim 80\%$ measured for the original annotations. Although these numbers are only approximate, as they were obtained by visual inspection, which is prone to bias, they suggest that performance indicators may be underestimated and could potentially be higher with more accurate initial data. This observation highlights one of the key strengths of deep learning models mentioned before: the ability to learn the correct prediction function, even in the presence of partially imperfect annotations.

3.2 Segmentation of galaxies based on U-Net

Our main motivation behind this work is the analysis of warps in edge-on galaxies, which we plan to present in a future work. Therefore, to analyse our detected galaxies, we need to segment the image and extract the galaxies, while removing nearby objects that might contaminate them. There are several methods of image segmentation, such as thresholding, when the object is selected based on having a significantly higher pixel intensity value than the background (e.g., Lotz et al. 2004; Zee et al. 2022), using isophotes to define the extent of the galaxy (e.g., Hao et al. 2006; Reshetnikov et al. 2016), deep learning (e.g., Boucaud et al. 2020; Farias et al. 2020) and other methods (for a comprehensive list of methods and their comparisons see Xu & Zhu 2024). Each method has its advantages and pitfalls,

but in all cases, determining the threshold where the galaxy ends and the background starts exactly can be challenging.

We decided to extract the galaxies using our own segmentation algorithm. We used the bounding box coordinates obtained from the YOLOv5 detection to accurately crop galaxies from the original images. This procedure ensured that the segmented images contained only relevant galaxy data, thus optimising the segmentation process.

The process of creating high-quality segmentation masks from cropped galaxy images was time-consuming, mainly due to the manual adjustment of parameters. Each iteration involved careful parameter settings for thresholding and morphological operations such as erosion and dilation. After setting these parameters, we manually checked the resulting masks to ensure that they met our standards for clarity and definition of galaxy structures.

This iterative process of checking, adjusting, and rechecking was necessary to achieve the desired quality of the segmentation masks. The challenges and steps associated with this procedure are shown in Fig. 5. The goal of each refinement was to remove the remaining irrelevant background noise and improve the edges of the galaxy structures, ensuring that the masks were best suited to train our segmentation models and to get as precise as possible final masks.

To automate the generation of segmentation masks, we used SCSS-Net, a convolutional neural network inspired by the U-Net architecture, originally designed to segment solar corona structures (Mack-

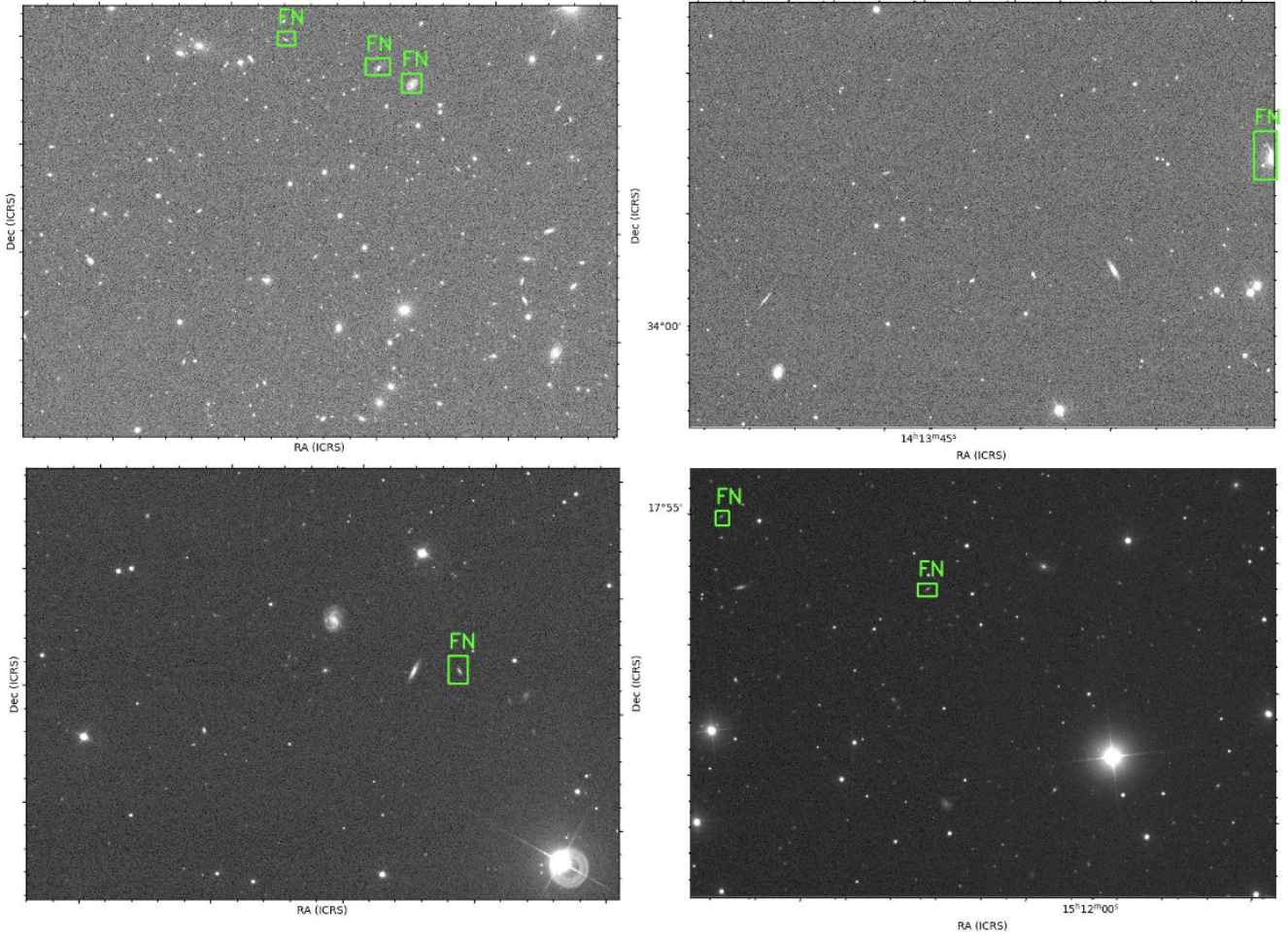


Figure 4. Examples of False Negatives Detected by YOLOv5. These often represent stars, incorrectly annotated by the annotators, confirming their classification as True Negatives, which in reality do not contribute to our detection metrics.



Figure 5. Gradual refinement of the segmentation mask for the galaxy. From left to right: Original galaxy image, initial segmentation mask, and refined segmentation mask after iterative parameter adjustment and noise removal.

ovjak et al. 2021). This versatile model was adapted for our specific requirement and retrained for segmentation of edge-on galaxies.

U-Net is a highly efficient convolutional neural network originally developed for medical image segmentation. Its architecture, designed to work effectively even with a limited amount of data, is characterised by its distinctive U-shape, comprising two main components: an encoder and a decoder (Ronneberger et al. 2015).

Encoder: The encoder is responsible for progressively capturing the context in the image, which involves reducing the spatial dimensions while increasing the depth. This process helps in extracting and compressing feature information, which is crucial for understanding the complex structures within the image.

Decoder: In contrast, the decoder part of the network works on

upsampling the feature map to reconstruct the image output. It progressively recovers the spatial dimensions and detail of the image, ensuring that the important features extracted by the encoder are used to generate a precise and detailed segmentation. In our case the input is the original galaxy image with our manually created mask and the output is the mask created by the algorithm.

This architecture not only allows detailed image segmentation but also ensures that the network learns from a relatively small amount of data, making it particularly powerful in fields where high-quality data is scarce.

For the segmentation model learning, we divided our dataset into training, validation, and test sets, and tuned basic hyperparameters such as image size, batch size, and number of epochs. Due to the small size of our images (64×64 pixels), the initial training phase was efficient. We aimed for 1,000 epochs with a batch size of 20, but concluded training at epoch 963 as performance gains plateaued.

Accurate evaluation is critical in the development and refinement of image segmentation models. The following metrics are commonly used to assess the quality and accuracy of segmentation results:

- **Intersection over Union (IoU):** Also known as the Jaccard Index, IoU is a statistical tool used to quantify the percent overlap between the target mask and the prediction output by the model. It is calculated as the area of overlap between the predicted segmen-

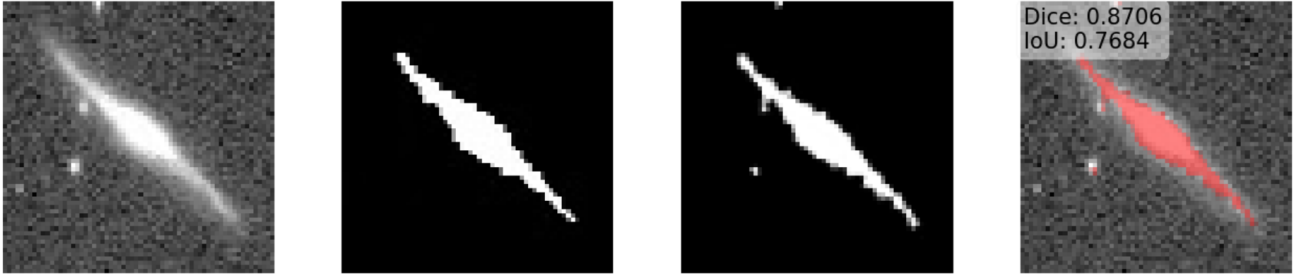


Figure 6. Detailed stages of galaxy image segmentation. From left to right: the original galaxy image, the ground truth mask, the segmentation result, and the final overlay highlighting the segmentation accuracy with performance metrics.

tation and the ground truth divided by the area of union between the predicted and ground truth. This metric is particularly useful for determining how well the predicted boundaries align with the true boundaries.

$$\text{IoU} = \frac{\text{Area of Overlap}}{\text{Area of Union}} \quad (5)$$

- **Dice Coefficient:** Similar to IoU, the Dice coefficient measures the similarity between two samples. It is defined as twice the area of overlap between the prediction and ground truth, divided by the total number of pixels in both the prediction and ground truth. This makes it a commonly used metric in medical image segmentation due to its sensitivity to small objects.

$$\text{Dice} = \frac{2 \times |\text{Prediction} \cap \text{Ground Truth}|}{|\text{Prediction}| + |\text{Ground Truth}|} \quad (6)$$

Testing revealed an average IoU of 0.75 and a Dice coefficient of 0.86, reflecting the efficiency of the model. Bright stars within the images were the main source of errors, a challenge we plan to address in the future. Despite these issues, the segmentation results were predominantly precise and well-defined. In segmentation tasks, we often see lower values of IoU and Dice score, which is caused by the fact that ground truth masks are manually or semi-manually produced (using some setup of selected thresholding and morphological operations), i.e., the ground truth masks are not ideal, but instead have some bias. However, deep learning is able to overcome such bias thanks to its learning capacity with more complex function defined by weights in its architecture and provide better segmentation results. Therefore, IoU and Dice will not reach optimal values, as they are measuring overlap with biased ground truth masks, but will be of relatively high value. In such cases, it is also important to do qualitative checks for final segmented masks and see whether these masks are mostly valid.

As illustrated in Fig. 6, the segmentation process is detailed through four sequential stages. The first panel shows the original galaxy image, followed by the ground truth mask in the second panel, which serves as the training and validation sample for the performance of our model. The third panel displays the result of the segmentation produced by our model, and the final panel overlays this segmentation on the original image to highlight the model’s accuracy and effectiveness. Notably, the Dice coefficient and IoU values, 0.87 and 0.77 respectively, demonstrate the high precision and effectiveness of our segmentation approach.

The model demonstrated reliability in its discrimination of relevant pixels for segmentation, often outperforming the quality of

our manual masks, as reflected in the metrics. An example of such segmentation and its validation is shown in Fig. 7. We found that combination of generally high scoring metrics and visual inspection of segmented edge-on galaxies showed good and stable results for final setup of algorithm.

After advanced segmentation techniques, the next key step was to extract relevant data from the FITS files using the resulting masks. This process is crucial to use our preprocessed galaxy images for further understanding and analysis. The result of this extraction can be seen in Fig. 8. This approach allows us to efficiently search existing galaxy databases and use the compiled data for a comprehensive analysis, which is detailed in the next section.

In Fig. 9 we illustrate the whole workflow of efficient processing of galaxy image data to ensure reliable preparation, modeling, and post-processing, developed in this work. This workflow is fundamental to understanding a systematic approach to the analysis of astronomical images and provides a clear path from raw data acquisition to the production of usable scientific data. To ensure complete transparency of our process and facilitate reproducibility, we provide comprehensive documentation, including all codes used in our analyses, available on our GitHub repository².

4 PROPERTIES OF THE SELECTED SAMPLE

In this section, we show some basic properties of the sample detected by our algorithm and show that in general they are of the same type of galaxies that we trained the algorithm on.

After segmentation and extraction of the galaxies from their fits files, we query their coordinates in the SDSS catalogue, retrieving their redshifts, magnitudes and b/a ratio using the *SciServer* package. We also retrieve the names of the galaxies from the NED database using the *astroquery* package (Ginsburg et al. 2019). In Table 3 we show the parameters of the first ten galaxies from our sample. The full table is available at our Github repository as well.

Then we calculate the absolute magnitudes using the usual formula

$$M = m - 25 - 5 \log_{10}(d(1+z)) - K, \quad (7)$$

where m is the Petrosian magnitude, corrected for the Galactic extinction using the map of Schlafly & Finkbeiner (2011), d is the comoving distance in Mpc, calculated using Python’s *astropy* package assuming flat Λ CDM cosmological model with total matter density and

² <https://github.com/MatFyzGalaxy/EdgeOnML>



Figure 7. Comparison of manual and automated segmentation techniques for a galaxy image. From left to right: the original galaxy image, the manual ground truth mask, the automated segmentation result, and an overlay highlighting the segmentation accuracy. The Dice coefficient is 0.6958 and the IoU is 0.5312, indicating that the automated segmentation outperforms the manual mask in defining galaxy structures.

Table 3. Selected parameters of the detected sample, taken from SDSS, unless stated otherwise. The full version of the table is available at our Github repository <https://github.com/MatFyzGalaxy/EdgeOnML>. Columns: (1): Unique SDSS identifier, (2): Galaxy name from NED, (3) and (4): J2000 coordinates, (5): Petrosian radius in the r band, (6)-(10): Petrosian flux in the respective bands, (7): Exponential fit b/a in the r band, (8): Redshift, (9): Confidence with which the galaxy was detected, given by the algorithm.

ID	$Name$	RA [deg]	DEC [deg]	u [mag]	g [mag]	r [mag]	i [mag]	z [mag]	$(b/a)_r$	$Redshift$	$Confidence$
1237667734496084000	UGC 05535	153.939	18.946	16.652	14.914	14.047	13.617	13.315	0.477	0.022	0.86
1237665228376899651	2MASS J11544292+3332148	178.680	33.537	17.963	15.543	14.762	14.315	14.002	0.220	0.032	0.86
1237661069790675120	NGC 3419A	162.833	14.023	15.783	14.694	14.263	14.046	13.825	0.197	0.010	0.85
1237661358608613531	UGC 05531	153.929	43.993	16.899	14.912	14.148	13.735	13.370	0.319	0.017	0.85
1237664671645368370	2MASS J13364223+3444493	204.175	34.746	16.480	14.706	13.903	13.466	13.192	0.386	0.024	0.84
1237662224593977484	2MASS J10211082+3539315	155.295	35.660	23.218	21.888	20.781	20.105	19.666	0.295	-	0.84
1237655126083043481	NGC 4252	184.629	5.559	15.665	14.516	14.126	13.871	13.777	0.312	0.003	0.84
1237662524157526119	2MASS J12412516+1343485	190.356	13.730	15.849	14.670	14.048	13.726	13.472	0.230	0.020	0.84
1237667142867615779	SDSS J092440.07+250642.6	141.167	25.110	16.339	14.574	13.698	13.227	12.885	0.414	0.027	0.84
1237667322179616901	2MASS J11425211+2632287	175.718	26.541	17.259	15.278	14.324	13.828	13.503	0.412	0.028	0.83



Figure 8. Illustration of image data extraction from FITS files, showing the accuracy and efficiency of the process.

dark energy density $\Omega_m = 0.27$, $\Omega_\Lambda = 0.73$ respectively and Hubble constant $H_0 = 70 \text{ km s}^{-1} \text{ Mpc}^{-1}$. K is the $k + e$ correction, where the k -correction was calculated using the calculator³ based on Chilingarian et al. (2010) and Chilingarian & Zolotukhin (2012) and the evolution correction was determined using the expression

$$E(z) = Q_0[1 + Q_1(z - z_0)](z - z_0) \quad (8)$$

³ <http://kcor.sai.msu.ru/>

from Blanton (2006), where $Q_0 = 2.8$, $Q_1 = -1.8$ and $z_0 = 0.1$. This formula was derived for the SDSS sample, with redshifts $0.05 < z < 0.15$, which is satisfied for our sample.

In Fig. 11 we show an example of randomly selected galaxies with the respective confidence given by the algorithm. By inspecting the galaxies visually, we can see that the algorithm is rather conservative, and galaxies that are clearly edge-on or highly inclined are detected with confidence $0.7 - 0.9$. Galaxies with confidence < 0.5 are mostly small and/or faint, therefore, their nature could be debated. The default confidence threshold for YOLOv5 is set to 0.25. This value determines the minimum confidence score required for the model to consider a detected object as valid. Adjusting this threshold can help balance between detecting all possible objects (sensitivity) and minimising FP (precision). After optimising on our validation dataset, we used an optimal confidence threshold of 0.3 to achieve a better balance between precision and recall, ensuring more reliable detections in our specific context. Therefore, we provide all galaxies detected with confidence > 0.3 , but for further astrophysical analysis we recommend using galaxies with confidence at least > 0.5 .

Looking closer at our sample of galaxies, in Fig. 12 we can see that our galaxies are nearby, with most of the redshifts being about $0.02 < z < 0.10$, which is expected for our sample and is in good agreement with the redshifts of the Galaxy Zoo sample that we used for training. In Fig. 13 we show the colour-magnitude diagram of our sample. We divide the magnitude into red, green and blue parts, based on criteria from Papastergis et al. (2013). Most of our galaxies are red, which may seem unexpected, since we are looking for spiral galaxies, but this result is in agreement with Makarov et al. (2022) who made a catalogue of 16,551 edge-on galaxies created using the

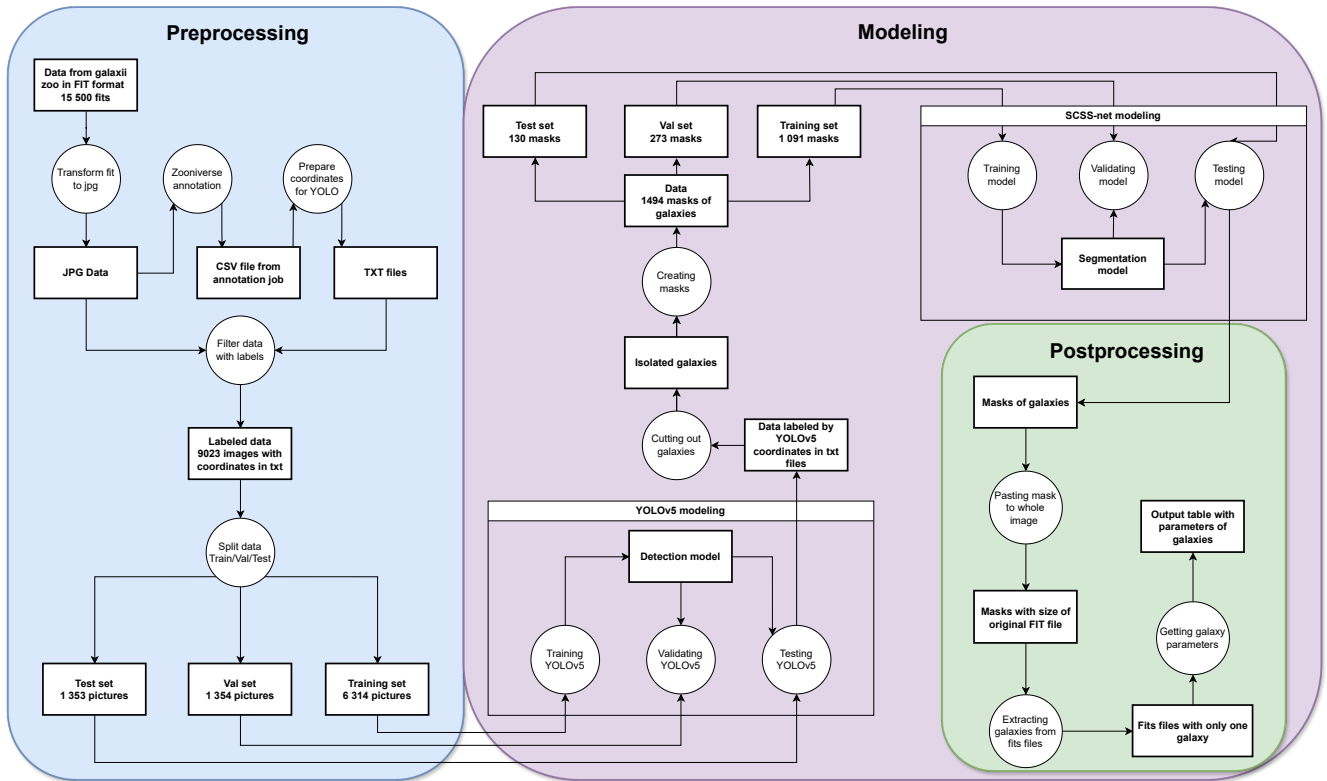


Figure 9. Diagram outlining the complete workflow used in the study, illustrating the process of data preparation, modelling and post-processing. Starting with the pre-processing phase, we transform the FITs data into JPEG format and annotate it, followed by splitting it into labeled datasets for machine learning training. The modeling phase involves training the YOLOv5 detection model and the SCSS-net segmentation model to identify and segment galaxies from astronomical images. The post-processing phase focuses on generating segmentation masks and extracting galaxy parameters for further analysis, demonstrating an integrated approach from raw data to usable scientific outputs.

public DR2 data of the Pan-STARRS survey. They show that edge-on galaxies are redder than general samples of galaxies containing all inclinations, due to internal extinction of edge-on galaxies, which is also why these galaxies are usually excluded when calculating Tully-Fisher relationship (see for example Karachentsev et al. 2002).

The minor to major axes ratio b/a , which can be seen in Fig. 14 is low for most detected galaxies, which is expected from edge-on galaxies and is in agreement with Makarov et al. (2022). We see that there are some outliers that seem thicker, which is due to several factors. Some galaxies detected by the algorithm are faint and/or blurry, especially those detected with lower confidence, therefore, they might have higher values of b/a . Moreover, our original sample of galaxies from Galaxy Zoo, which might have some annotation bias, has similar distribution of b/a , so our algorithm is detecting galaxies similar to what it was trained on. Another point is that some galaxies that have a relatively high value of b/a in the SDSS catalogue appear as thin and edge-on or highly inclined. We illustrate this in Fig. 10, where we show some examples of galaxies with $0.35 < (b/a)_r < 0.39$, although they appear as thin and edge-on, therefore, the algorithm detected them correctly.

Makarov et al. (2022) also found that on average, red galaxies are thicker than blue ones. In order to corroborate this, we plot a normalised histogram of inverse galaxy thickness in Fig. 15 for the red and blue populations separately. We see that our red population reaches a bit higher values of thickness, however the maximum of both red and blue sample lies around the same value of a/b and the difference between the samples is rather small. Moreover, the

sample of blue galaxies is quite smaller than the red sample, which may bias a direct comparison, therefore, we cannot make a definitive conclusion about the colour-thickness relationship.

5 CONCLUSIONS

We present a novel deep learning algorithm for the detection and extraction of edge-on galaxies in astronomical images. Based on Galaxy Zoo classification, we obtained images of approximately 16,000 edge-on, spiral galaxies from the SDSS catalogue, that we trained the algorithm on. Our results show that the algorithm can reliably detect edge-on galaxies, with Precision=0.80 and Recall=0.94. We also successfully applied a segmentation algorithm to extract the galaxies from the image, so they can be used for future studies. We retrieved the parameters of our sample of galaxies from the SDSS and provide them together with confidence values. From a basic analysis of the properties of our sample, we find that the majority of galaxies is nearby ($0.02 < z < 0.10$), red and have low values of b/a , which is in agreement with other works. Our analysis of the SDSS data showed that we can reliably detect the needed galaxies, however, the true potential of the algorithm lies in its possible application on data from future surveys, such as Euclid (Euclid Collaboration et al. 2024), Roman Space Telescope (Bartusek et al. 2022) or Large Synoptic Survey Telescope (LSST, Ivezić et al. 2019) where we expect a significant increase in data volume, which necessitates processing through machine learning.

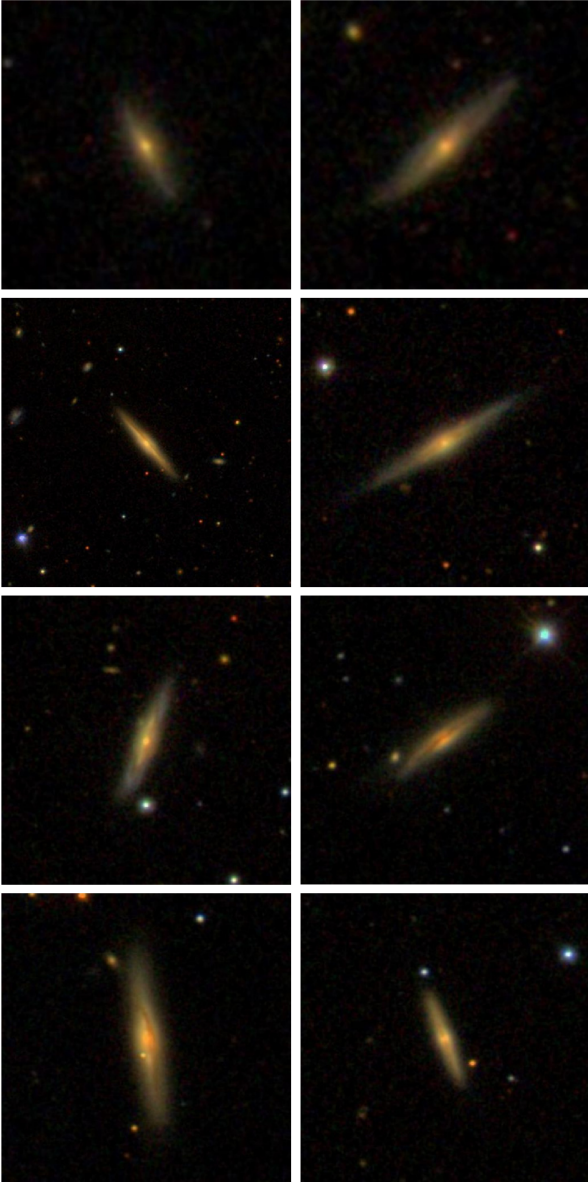


Figure 10. Example of several galaxies detected by our algorithm, that have high values of b/a ratio, despite looking like edge-on galaxies. All galaxies shown above have $0.35 < (b/a)_r < 0.39$.

ACKNOWLEDGEMENTS

We thank Daisuke Kawata, Ralph Schönrich and Mat Page for useful advice and comments. Z.C. was supported by Royal Society grant No. UF160158/ RFVERE\210415. V.K. and P.B. were supported by VEGA—the Slovak Grant Agency for Science, grant No. 1/0685/21. R.N. was supported by VEGA—the Slovak Grant Agency for Science, grant No. 1/0761/21, and by the Erasmus+ programme of the European Union under grant No. 2020-1-CZ01-KA203-078200. This research made use of the “K-corrections calculator” service available at <http://kcor.sai.msu.ru/>. Funding for the Sloan Digital Sky Survey (SDSS) and SDSS-II has been provided by the Alfred P. Sloan Foundation, the Participating Institutions, the National Science Foundation, the U.S. Department of Energy, the National Aeronautics and Space Administration, the Japanese Monbukagakusho, and the Max Planck Society, and the Higher Education Funding Council

for England. The SDSS Web site is <http://www.sdss.org/>. The SDSS is managed by the Astrophysical Research Consortium (ARC) for the Participating Institutions. The Participating Institutions are the American Museum of Natural History, Astrophysical Institute Potsdam, University of Basel, University of Cambridge, Case Western Reserve University, The University of Chicago, Drexel University, Fermilab, the Institute for Advanced Study, the Japan Participation Group, The Johns Hopkins University, the Joint Institute for Nuclear Astrophysics, the Kavli Institute for Particle Astrophysics and Cosmology, the Korean Scientist Group, the Chinese Academy of Sciences (LAMOST), Los Alamos National Laboratory, the Max-Planck-Institute for Astronomy (MPIA), the Max-Planck-Institute for Astrophysics (MPA), New Mexico State University, Ohio State University, University of Pittsburgh, University of Portsmouth, Princeton University, the United States Naval Observatory, and the University of Washington. This publication uses data generated via the Zooniverse.org platform, development of which is funded by generous support, including a Global Impact Award from Google, and by a grant from the Alfred P. Sloan Foundation.

DATA AVAILABILITY

The catalogue of galaxies generated in this work is available at our Github repository <https://github.com/MatFyzGalaxy/EdgeOnML>.

REFERENCES

- Abazajian K. N., et al., 2009, *ApJS*, **182**, 543
 Abraham S., Aniyani A. K., Kembhavi A. K., Philip N. S., Vaghmare K., 2018, *MNRAS*, **477**, 894
 Andika I. T., et al., 2023, *A&A*, **678**, A103
 Banerji M., et al., 2010, *MNRAS*, **406**, 342
 Barchi P. H., et al., 2020, *Astronomy and Computing*, **30**, 100334
 Barteldrees A., Dettmar R. J., 1994, *A&AS*, **103**, 475
 Bartusek L. M., Davis J. L., Vess M. F., 2022, in 2022 IEEE Aerospace Conference (AERO), pp 01–14, doi:10.1109/AERO53065.2022.9843415
 Bizyaev D. V., Kautsch S. J., Mosenkov A. V., Reshetnikov V. P., Sotnikova N. Y., Yablokova N. V., Hillyer R. W., 2014, *ApJ*, **787**, 24
 Blanton M. R., 2006, *ApJ*, **648**, 268
 Bonjean V., Aghanim N., Salomé P., Beelen A., Douspis M., Soubrié E., 2019, *A&A*, **622**, A137
 Bonnett C., 2015, *MNRAS*, **449**, 1043
 Boucaud A., et al., 2020, *MNRAS*, **491**, 2481
 Bregman J. N., 1980, *ApJ*, **236**, 577
 Bregman J. N., Houck J. C., 1997, *ApJ*, **485**, 159
 Burstein D., 1979, *ApJ*, **234**, 829
 Chang Y.-Y., Lin L., Pan H.-A., Lin C.-A., Hsieh B.-C., Bottrell C., Wang P.-W., 2022, *ApJ*, **937**, 97
 Cheng T.-Y., Li N., Conselice C. J., Aragón-Salamanca A., Dye S., Metcalf R. B., 2020, *MNRAS*, **494**, 3750
 Chilingarian I. V., Zolotukhin I. Y., 2012, *MNRAS*, **419**, 1727
 Chilingarian I. V., Melchior A.-L., Zolotukhin I. Y., 2010, *MNRAS*, **405**, 1409
 Chu J., Tang H., Xu D., Lu S., Long R., 2024, *MNRAS*, **528**, 6354
 Collister A. A., Lahav O., 2004, *PASP*, **116**, 345
 Comerón S., et al., 2011, *ApJ*, **738**, L17
 D’Isanto A., Polsterer K. L., 2018, *A&A*, **609**, A111
 Davidzon I., et al., 2022, *A&A*, **665**, A34
 Dieleman S., Willett K. W., Dambre J., 2015, *MNRAS*, **450**, 1441
 Euclid Collaboration et al., 2024, *arXiv e-prints*, p. arXiv:2405.13491
 Fariás H., Ortiz D., Damke G., Jaque Arancibia M., Solar M., 2020, *Astronomy and Computing*, **33**, 100420

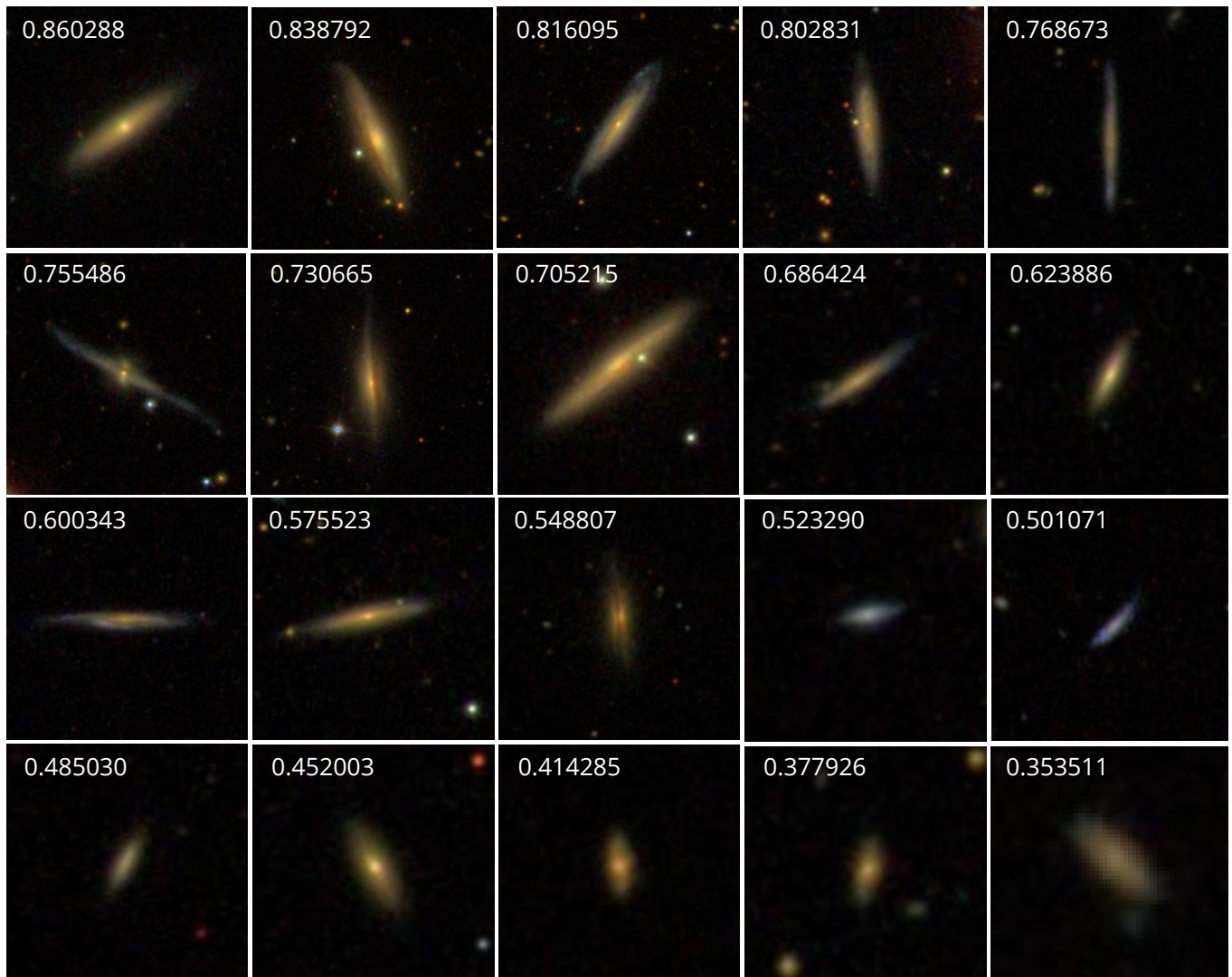


Figure 11. Examples of randomly selected detected galaxies, with various confidence values.

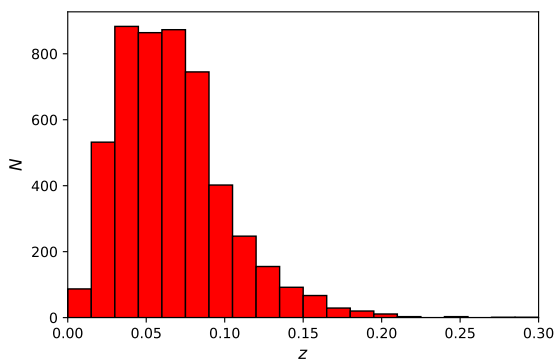


Figure 12. Distribution of redshifts of the sample.

Ferreira L., Conselice C. J., Duncan K., Cheng T.-Y., Griffiths A., Whitney A., 2020, *ApJ*, **895**, 115
 Fraternali F., Oosterloo T. A., Sancisi R., Swaters R., 2005, in Braun R., ed., *Astronomical Society of the Pacific Conference Series*

Vol. 331, Extra-Planar Gas. p. 239 ([arXiv:astro-ph/0410375](https://arxiv.org/abs/astro-ph/0410375)), [doi:10.48550/arXiv.astro-ph/0410375](https://doi.org/10.48550/arXiv.astro-ph/0410375)

Gharat S., Dandawate Y., 2022, *MNRAS*, **511**, 5120

Ghosh A., Urry C. M., Wang Z., Schawinski K., Turp D., Powell M. C., 2020, *ApJ*, **895**, 112

Ghosh A., et al., 2022, *ApJ*, **935**, 138

Gilhuly C., et al., 2022, *The Astrophysical Journal*, 932

Ginsburg A., et al., 2019, *AJ*, **157**, 98

González R. E., Muñoz R. P., Hernández C. A., 2018, *Astronomy and Computing*, **25**, 103

Hamabe M., Kodaira K., Okamura S., Takase B., 1979, *PASJ*, **31**, 431

Hao C. N., Mao S., Deng Z. G., Xia X. Y., Wu H., 2006, *MNRAS*, **370**, 1339

Hodges-Kluck E. J., Bregman J. N., 2012, *The Astrophysical Journal*, 762

Howk J. C., Savage B. D., 1997, *AJ*, **114**, 2463

Howk J. C., Savage B. D., 1999, *AJ*, **117**, 2077

Ivezić Ž., et al., 2019, *ApJ*, **873**, 111

Jocher G., et al., 2020, *ultralytics/yolov5: v3.1 - Bug Fixes and Performance Improvements*, [doi:10.5281/zenodo.4154370](https://doi.org/10.5281/zenodo.4154370), <https://doi.org/10.5281/zenodo.4154370>

Kaiser N., et al., 2010, in Stepp L. M., Gilmozzi R., Hall H. J., eds, *Society of Photo-Optical Instrumentation Engineers (SPIE) Conference Series Vol. 7733, Ground-based and Airborne Telescopes III*. p. 77330E, [doi:10.1117/12.859188](https://doi.org/10.1117/12.859188)

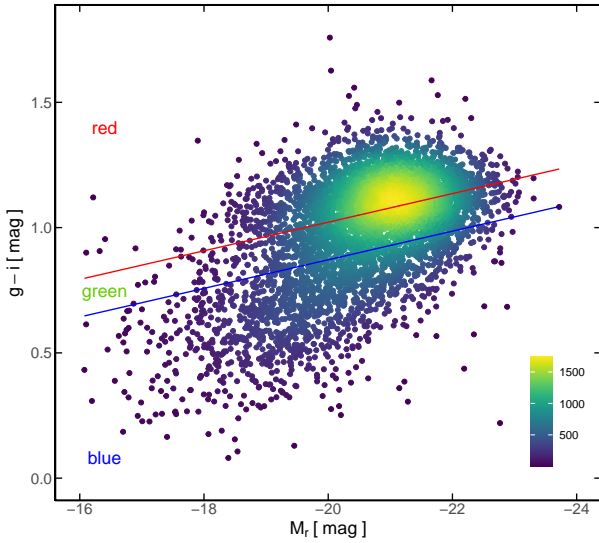


Figure 13. Galaxy colour-magnitude diagram for our sample, separated into red, green and blue areas, using only galaxies for which the redshift is known. The colours were corrected for Galactic extinction and K correction as described in Section 4. The red line is defined as $g-i = -0.0571(M_r + 24) + 1.2$, while the blue line is offset by 0.15 mag (Papastergis et al. 2013)

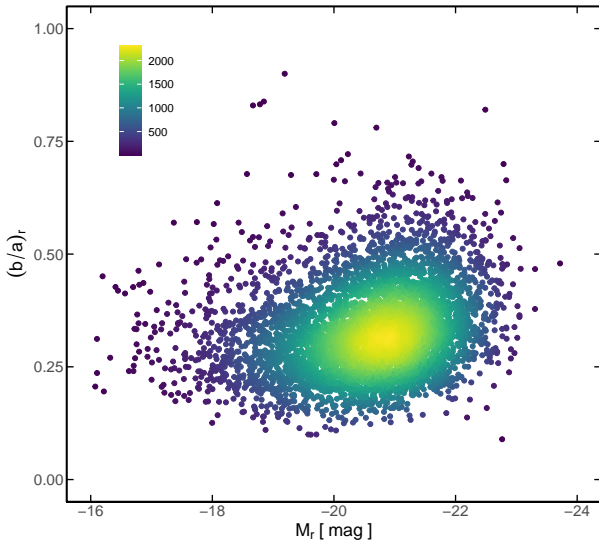


Figure 14. Minor to major axes ratio as a function of absolute magnitude, using only galaxies for which the redshift is known.

Karachentsev I. D., Mitronova S. N., Karachentseva V. E., Kudrya Y. N., Jarrett T. H., 2002, *A&A*, 396, 431
 Kautsch S. J., Grebel E. K., Barazza F. D., Gallagher J. S. I., 2006, *A&A*, 445, 765
 Kormendy J., Bruzual A. G., 1978, *ApJ*, 223, L63
 Kregel M., van der Kruit P. C., 2004, *MNRAS*, 352, 787
 La Torre V., Sajina A., Goulding A. D., Marchesini D., Bezanson R., Pearl A. N., Sodré Laerte J., 2024, *arXiv e-prints*, p. arXiv:2403.18888
 Lee S.-W., Irwin J. A., 1997, *ApJ*, 490, 247
 Levy R. C., et al., 2019, *The Astrophysical Journal*, 882
 Liew-Cain C. L., Kawata D., Sánchez-Blázquez P., Ferreras I., Symeonidis M., 2021, *MNRAS*, 502, 1355
 Lin Q., Fouchez D., Pasquet J., Treyer M., Ait Ouahmed R., Arnouts S., Ilbert O., 2022, *A&A*, 662, A36

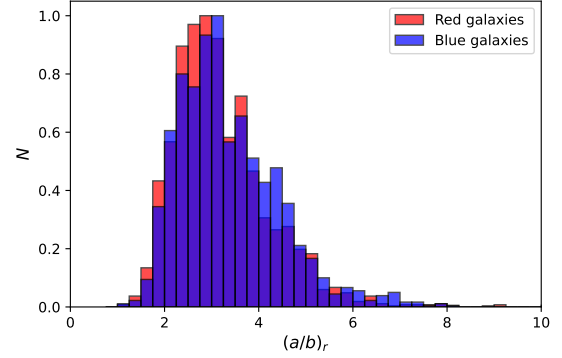


Figure 15. Normalised histogram of the inverse thickness of the galaxies for red and blue galaxies. The galaxies were separated as in Fig. 13.

Lintott C. J., et al., 2008, *MNRAS*, 389, 1179
 Lotz J. M., Primack J., Madau P., 2004, *AJ*, 128, 163
 Mackovjak Š., Harman M., Maslej-Krešňáková V., Butka P., 2021, *MNRAS*, 508, 3111
 Makarov D. I., Burenkov A. N., Tyurina N. V., 1999, *Astronomy Letters*, 25, 706
 Makarov D., et al., 2022, *MNRAS*, 511, 3063
 Martínez-Lombilla C., Trujillo I., Knapen J. H., 2019, *MNRAS*, 483, 664
 Mosenkov A., et al., 2020, *MNRAS*, 494, 1751
 Mosenkov A. V., et al., 2022, *MNRAS*, 515, 5698
 Mouhcine M., Rejkuba M., Ibata R., 2007, *MNRAS*, 381, 873
 Omori K. C., et al., 2023, *A&A*, 679, A142
 O'Brien J. G., Kerin W. M., Chiarelli T. L., 2023, *Journal of Physics: Conference Series*, 2482
 Papastergis E., Giovanelli R., Haynes M. P., Rodríguez-Puebla A., Jones M. G., 2013, *ApJ*, 776, 43
 Pearson W. J., Wang L., Trayford J. W., Petrillo C. E., van der Tak F. F. S., 2019, *A&A*, 626, A49
 Peruzzi T., Pasquato M., Ciroi S., Berton M., Marziani P., Nardini E., 2021, *A&A*, 652, A19
 Pildis R. A., Bregman J. N., Schombert J. M., 1994, *The Astrophysical Journal*, 427, 160
 Pohlen M., Dettmar R. J., Lütticke R., 2000, *A&A*, 357, L1
 Pohlen M., Dettmar R. J., Lütticke R., Aronica G., 2002, *A&A*, 392, 807
 Reach W. T., Fadda D., Rand R. J., Stacey G. J., 2020, *ApJ*, 902, 28
 Redmon J., Divvala S., Girshick R., Farhadi A., 2016, in *Proceedings of the IEEE conference on computer vision and pattern recognition*. pp 779–788
 Reshetnikov V., Combes F., 1998, *A&A*, 337, 9
 Reshetnikov V. P., Mosenkov A. V., Moiseev A. V., Kotov S. S., Savchenko S. S., 2016, *MNRAS*, 461, 4233
 Rezaei S., McKean J. P., Biehl M., de Roo W., Lafontaine A., 2022, *MNRAS*, 517, 1156
 Ronneberger O., Fischer P., Brox T., 2015, in *Medical image computing and computer-assisted intervention—MICCAI 2015: 18th international conference, Munich, Germany, October 5-9, 2015, proceedings, part III*. pp 234–241
 Salo H., et al., 2015, *ApJS*, 219, 4
 Sancisi R., 1976, *A&A*, 53, 159
 Savchenko S. S., Makarov D. I., Antipova A. V., Tikhonenko I. S., 2024, *Astronomy and Computing*, 46, 100771
 Schlafly E. F., Finkbeiner D. P., 2011, *ApJ*, 737, 103
 Scoville N., et al., 2007, *ApJS*, 172, 1
 Seth A. C., Dalcanton J. J., de Jong R. S., 2005, *AJ*, 130, 1574
 Shi F., Liu Y.-Y., Li P.-Y., Yu M., Lei Y.-M., Wang J., 2015, *MNRAS*, 451, 629
 Shinn J.-H., 2018, *ApJS*, 239, 21
 Storrie-Lombardi M. C., Lahav O., Sodre L. J., Storrie-Lombardi L. J., 1992, *MNRAS*, 259, 8P

- Surana S., Wadadekar Y., Bait O., Bhosale H., 2020, *MNRAS*, **493**, 4808
- Tarsitano F., Bruderer C., Schawinski K., Hartley W. G., 2022, *MNRAS*, **511**, 3330
- Tikhonov N. A., Galazutdinova O. A., 2005, *Astrophysics*, **48**, 221
- Usachev P. A., Reshetnikov V. P., Savchenko S. S., 2024, *MNRAS*, **529**, L78
- Vergani D., Gentile G., Dettmar R. J., Aronica G., Klein U., 2003, *Astronomische Nachrichten Supplement*, **324**, 88
- Vijayakumar A., Vairavasundaram S., 2024, *Multimedia Tools and Applications*, pp 1–40
- Wilde J., Serjeant S., Bromley J. M., Dickinson H., Koopmans L. V. E., Metcalf R. B., 2022, *MNRAS*, **512**, 3464
- Willett K. W., et al., 2013, *MNRAS*, **435**, 2835
- Wu Y., Tao Y., Fan D., Cui C., Zhang Y., 2024, *MNRAS*, **527**, 1163
- Xu D., Zhu Y., 2024, *Astronomy and Computing*, **48**, 100838
- Zee W.-B. G., Yoon S.-J., Moon J.-S., An S.-H., Paudel S., Yun K., 2022, *ApJ*, **935**, 48
- Zhang K., Schlegel D. J., Andrews B. H., Comparat J., Schäfer C., Vazquez Mata J. A., Kneib J.-P., Yan R., 2019, *ApJ*, **883**, 63
- Zibetti S., Ferguson A. M. N., 2004, *MNRAS*, **352**, L6
- de Grijs R., van der Kruit P. C., 1996, *A&AS*, **117**, 19
- van der Kruit P. C., 2007, *A&A*, **466**, 883
- van der Kruit P. C., Searle L., 1981, *A&A*, **95**, 105

This paper has been typeset from a $\text{\TeX}/\text{\LaTeX}$ file prepared by the author.